Electrochimica Acta 437 (2023) 141532

Contents lists available at ScienceDirect

Electrochimica Acta

journal homepage: www.journals.elsevier.com/electrochimica-acta

Fabrications of Sb@rGO@NSC composite materials as anodes with high performance for lithium ion batteries

Yuan Mu [a], Dakui Zhang [c], Jianke Li [a], Beibei Han [b,d], Guiying Xu [a,*], Kun Wang [a,*], Baigang An [a], Dongying Ju [b,e], Lixiang Li [a], Weimin Zhou [a,*]

[a] Key Laboratory of Energy Materials and Electrochemistry Research Liaoning Province, University of Science and Technology Liaoning, No. 189, Qianshan Middle Road, Lishan District, Anshan, Liaoning 114051, China
[b] Advanced Science Research Laboratory, Saitama Institute of Technology, Fukaya, Fusaiji 1690, Japan
[c] Angang Chemical Technology Co., Ltd in Anshan Iron and Steel Plant, Tiexi District, Anshan 114011, China
[d] Key Laboratory of Advanced Fuel Cells and Electrolyzers Technology of Zhejiang Province, Ningbo Institute of Materials Technology and Engineering, Chinese Academy of Sciences, Ningbo, No. 1219 Zhongguan West Road, Zhejiang 315201, China
[e] Hainai University, 58 Renmin Avenue, Haikou 570228, China

ARTICLE INFO

Keywords:
Sb
Composite materials
High performance
3D hierarchical porous structures
Lithium ion batteries (LIBs)

ABSTRACT

In accordance with a double covering idea, the Sb@rGO@NSC (Sb covered by rGO and N, S doped carbons) with high performance is successfully synthesized by co-carbonizations using the $SbCl_3$, GO, glucose, ammonium citrate and sulfocarbamide. The tremendous dispersions of Sb particles with nano sizes in carbon substrates and formations of 3D hierarchical porous structures make the Sb@rGO@NSC-0.3 composite material to possess the superior electrochemical performance. As can be seen, the Sb@rGO@NSC-0.3 manifests the high storage capacity (1121.2 mAh g^{-1}) at 0.5 A g^{-1}, over cycling 500 times. Concurrently, the storage capacity of Sb@rGO@NSC-0.3 has 721.1 mAh g^{-1} and 342.9 mAh g^{-1}, even after carrying out the cycles 1000 times with current densities set as 1.0 A g^{-1} and 5.0 A g^{-1}, respectively. The structural merits of Sb@rGO@NSC-0.3 can lead contents of Sb and contained carbons to develop their fundamental storage abilities as far as possible, which is a reason that the Sb@rGO@NSC-0.3 possesses exceedingly competitive storage performance.

1. Introduction

Nowadays, lithium-ion batteries (LIBs) as a marketable commodity have largely dominated the fields of electrical products such as portable electronics, electric vehicles (EVs) markets, energy storage systems (ESSs) and so on [1–3]. Nevertheless, with the explosive developments of the energy storage systems, the issue of how to contribute the excellent performance such as high mass energy density, power density, and long-term cycling stability under high currents to LIBs has received considerably critical attentions from manufacturers. Thus, fabricating electrodes with highly electrochemical performance has become of an important component in fabrication fields of electrodes of LIBs [4,5].

Using metals and metal oxides as negative electrodes is a popular idea to improve the storage capacity of negative electrodes due to their extremely high theoretical capacity [6,7]. Among them, Si/C composite materials have attracted widespread attentions because the Si possesses significantly high theoretical capacity of 4200 mAh g^{-1} [8–10]. However, the electrochemical instabilities under high current densities gravely restrain the application scenarios of Si/C composite materials [11]. On the other hand, covering the carbon materials on the surface of metal oxides is an effective way to create anodes with high storage capacity [12–14]. Because of the fact that covering method can restrict the volumetric expansion not only, but also the conductivity is able to be improved by introducing the carbons. Nevertheless, the high charge-discharge plateaus of a part of metal oxides such as Fe_3O_4, FeO, SnO_2 and NiO influence the power densities of assembled full cells [15–18]. Zhang et al. also pointed out that such materials would need to exceed specific capacity of 1000 mAh/g, in order to challenge the commercial graphite anode [19]. Therefore, fabricating the negative electrodes having the merits such as long cycle performance at big current densities, greatly high storage capacity and low charge-discharge plateaus are an extremely pivotal challenges in a number of research groups.

In recent years, the Sb has drown more attention in fabrications of

* Corresponding authors.
E-mail addresses: xuguiying751107@163.com (G. Xu), ustl15542731203@163.com (K. Wang), aszhou15242870697@163.com (W. Zhou).

https://doi.org/10.1016/j.electacta.2022.141532
Received 5 September 2022; Received in revised form 30 October 2022; Accepted 11 November 2022
Available online 16 November 2022

electrodes of LIBs due to its advantages such as high theoretical capacity (660 mAh g^{-1}), suitable intercalation potential (0.8~0.9 V), low polarization voltage (~0.2 V) and so on [20–22]. In addition, compared with the Si, Ge and Sn, the layered fold structures on Sb lead it to possess the suitable space to store Li^+ not only, but the conductivity of Sb can also be improved [23]. However, the structural collapse of Sb also exists in the charge-discharge processes, similar to the general storage type as an alloy reaction of metal and metal oxides [23–25].

On the basis of aforementioned descriptions, it is naturally considerable that covering carbons on the surface of Sb is efficacious way to develop the storage capacity of Sb. However, carrying out the carbon covering once is not enough because the existed collapse phenomena of metal and metal oxides can not be avoided thoroughly, which causes that the prepared composite materials have not ideal storage capacity [25–26]. To improve the covering effects, the secondary covering on the basis of the first one is a conceivable way to improve the covering effect so as to develop the storage capacity of metal or metal oxides in metal or metal oxides / carbon composite materials.

Furthermore, doping the N and S elements in carbon structures is another effective way to enhance the storage capacity of carbon materials because the doped N and S elements can improve the infiltration of electrolyte not only, but also expand the space of structures of carbons to enhance the storage capacity of Li^+ [27].

Inspiring by the above discussions, in our studies, the Sb@rGO@NSC-X materials with 3D structures are fabricated by using the $SbCl_3$, GO, glucose, ammonium citrate and sulfocarbamide, in accordance with the sedimentation and hydrothermal method. Combined with detailed electrochemical evaluations, it is observed that the fabricated Sb@rGO@NSC materials manifest the extremely high storage capacity. As proof, the Sb@rGO@NSC-0.3 exhibits the high storage capacity (1151.3 mAh g^{-1}) over 100 cycles at 0.1 A g^{-1}. Additionally, when the current densities were respectively increased to the 1 A g^{-1} and 5 A g^{-1}, the storage capacity of 721.1 mAh g^{-1} and 342.9 mAh g^{-1} of Sb@rGO@NSC-0.3 can be achieved, indicating that the Sb@rGO@NSC-0.3 possesses the extremely fabulous long-term cycling stability at high current densities.

Based on the considerations regarding to the structure-activity relationship, it is considered that the exceedingly good dispersion of Sb particles and 3D hierarchical porous structures formed by existence of GO cause the impressive synergies between two contents of Sb and carbons in Sb@rGO@NSC-X composite materials, which leads Sb@rGO@NSC-X to have exceedingly tremendous storage capacity.

2. Experiment

2.1. Characteristics

The measurements of X-ray diffraction (XRD) were performed by the X'pert Powder instrument from PANalytical. The X-ray photoelectron spectroscopy (XPS) measurements were carried out on a K-Alpha instrument from Thermo Fisher Scientific, USA. Nitrogen adsorption and desorption isotherms was measured by a Quadrasorbautosorb-iQ surface analyzer which was purchased from Quantachrome Instruments, USA. Specific surface areas were determined in detail, according to the Brunauer-Emmett-Teller (BET) method. The pore size distribution was assessed by a density functional theory (DFT) model for slit pores. Thermogravimetry (TG) measurements were recorded using a Rigaku TG-DTA8122 thermal analyzer under a flow of air with a heating rate of 10 °C/min in a temperature range (25 °C-700 °C). Morphologies were evaluated by scanning electron microscopy (SEM) using an instrument produced by Carl Zeiss AG, Germany). LAND CT-3001A battery testing system was used to test the electrochemical performance of the buckle battery. Cyclic voltammetry and electrochemical impedance spectroscopy (over a frequency range of 100 kHz-0.01 Hz and the amplitude was 5 mV) were tested by CHI660E electrochemical workstation (ChenHua, Shanghai, China).

2.2. Synthesis of a GO based intermediate containing SbO_x

The graphene oxide (GO) (0.1 g) was dispersed in an alcohol solution (80 mL). The hexadecyl trimethyl ammonium bromide (CTAB) (0.3 g) was added in the solution containing GO. The obtained mixture was mixed by ultrasonic for 30 min, and obtained homogeneous solution was named as **α** solution. The $SbCl_3$ (8 mmol) was added into an alcohol solution (20 mL). The formed colorless transparent solution was named **β** solution. And then the **β** solution was dripped into the **α** solution with stirring. After dripping, the mixture solution was continuously stirred for 2 h, and it was filtered by a centrifugal separation to remove the unreacted antimonic salts.

2.3. Synthesis of Sb@rGO@NSC-X composite materials

The synthesized intermediate was dispersed in the deionized water (20 mL) by the ultrasonic for 30 min, and the obtained mixture solution was named as the **γ** solution. The glucose (0.1 g, 0.3 g or 0.5 g), ammonium citrate (0.2 g) and sulfocarbamide (1.8 g) were dissolved in the deionized water (30 ml), and this mixture solution was added into the **γ** solution. The obtained mixture solution was added into a reactor, and the reaction was carried out for 12 h at 90 °C. After cooling down to the room temperature, the dark solids were obtained by filtration and placed in a drying oven for 12 h at 90 °C.

The obtained solids were placed in a quartz crucible, which was placed in a tube furnace. The heating temperature of tube furnace was risen to 550 °C with a heating rate of 3 °C/min, and maintained at 550 °C for 2 h. According to the dosages of glucose, the names of obtained composite materials were decided as Sb@rGO@NSC-X (X = 0.1, 0.3 or 0.5 of glucose dosages).

2.4. Electrochemical measurements

The half-cells were prepared using the Sb@rGO@NSC-X composite materials. The Sb@rGO@NSC-X (70 mg) was mixed with the acetylene black (15 mg) and polyvinylidine fluoride (PVDF) binder (15 mg) in a weight ratio of 70:15:15 in N-methyl-2-pyrrolidone (NMP) solution. The obtained slurry was coated on the Cu foil and dried in a vacuum drying oven at 80 °C for 1 h to remove the solution. Subsequently, the Cu foil with the active materials was dried at 120 °C for 12 h in the same vacuum drying oven and cut into round shape strips of φ 11 mm in size. The mass loading of the active materials was controlled at 0.80 mg/cm^2. The two-electrode electrochemical cells (CR2032 coin-type) were assembled in a glove box filled with high-purity argon, in which cells were assembled using the lithium metal foil (φ 15.60 mm × 0.45 mm) as a reference electrode, Celgard 2400 micro-porous membrane as a separator, and 1 M $LiPF_6$ in the mixture of EC/DMC (1:1, vol%) with 5 vol% fluoroethylene carbonates (FEC) as electrolyte. Galvanostatic charge-discharge test was carried out by LAND (CT 3001A) battery test system in the voltage range of 0.01–3.00 V. The CV curves were recorded in the voltage region of 0.01–3.00 V at a scan rate of 0.2 mV/s. The impedance spectra were recorded in a frequency range of 100 kHz–0.01 Hz.

3. Results and discussion

The fabrications and structural imagination of Sb@rGO@NSC-X are visualized as shown in Fig. 1. In particular, in order to understand structure of Sb@rGO@NSC-X better, a pie imagination was used to be a referable reference. The carbon contents in fabricated Sb@rGO@NSC-X materials were firstly verified by the TGA measurements (Fig. 2a). The remarkable weight losses in 300–600 °C are generally attributed to the burning of carbon and oxidations of Sb to Sb_2O_4 [24]. It is observed that the weight losses of Sb@rGO@NSC-0.1, Sb@rGO@NSC-0.2 and Sb@rGO@NSC-0.3 were 52.5%, 63.6% and 78.4%, respectively (The names of Sb@rGO@NSC-X composite materials are confirmed in the

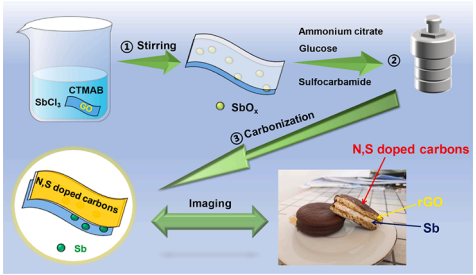

Fig. 1. Fabrications and imaginations of Sb@rGO@NSC-X materials.

Experimental section). After calculation, the carbon contents in Sb@rGO@NSC-X materials are 62.4%, 71.2% and 82.9%, respectively.

To acquire a better understanding of the structures and characteristics of Sb@rGO@NSC-X, as a contrast, the N, S doped GO carbon materials (rGO/NSC) were also fabricated by the same synthesization process with Sb@rGO@NSC-X materials. The N and S contents were evaluated by the elemental analysis (Table S1). Similar to reports by Chen et al., the pure Sb was also prepared in our studies so as to better conduct the comparisons of Sb@rGO@NSC-X with Sb [28]. The structures of Sb, rGO/NSC and Sb@rGO@NSC-X materials were investigated by the XRD measurements (Fig. 2b). It is found that the GO changed to the rGO, in agreement with a report by Mhamane et al. [14]. The (002) peaks of 25.7° and (100) peaks of 42.7° are observed in the rGO/NSC materials, indicating that it is in an amorphous statue [29]. In accordance with the standard card of ICDD 01–085–1322, it is observed that Sb clearly exists in the Sb@rGO@NSC-0.1 and Sb@rGO@NSC-0.3 materials. The phenomenon that the peak of Sb was not clearly observed in the Sb@rGO@NSC-0.5 is probably attributed to the peaks of Sb being covered by the carbon peaks due to the over-adding of glucose.

The structures of Sb, rGO/NSC and Sb@rGO@NSC-X materials were further surveyed by the Raman measurements (Fig. 2c). It is distinctly observed that the characteristic peak attributing to the Sb also exists in the Sb@rGO@NSC-X materials. Meanwhile, the characteristic peaks of general carbon materials in Sb@rGO@NSC-X materials are also verified at 1327 cm^{-1} and 1569 cm^{-1}, which correspond to the D and G peaks, respectively [30]. As shown in Table S2, the I_D/I_G values of Sb@rGO@NSC-0.1, Sb@rGO@NSC-0.3 and Sb@rGO@NSC-0.5 are 1.39, 1.44 and 1.35, respectively, revealing that Sb@rGO@NSC-0.3 possesses the more disordered structures than others [31].

The morphologies of Sb@rGO@NSC-X materials are described by SEM measurements (Figs. 3a–g and S1). It is observed that the 3D porous structures were constructed by the surrounding of lamellar structures (Figs. 3a–c and S1c–h). These structures are conducive to accelerate the rapid penetration of electrolytes and Li^+ transfer [32]. Compared to the Fig. S1d, it is thought that lamellar structures are mainly brought by rGO in composites, indicating that rGO exists in the Sb@rGO@NSC-X from another perspective. SEM-EDS images reveal that N and S elements dispersed in the Sb@GO@NSC-0.3 homogeneously (Fig. 3d–g). Especially, it is observed that some of the spherical substances exist in the Sb@GO@NSC-0.5 Fig. S1g. On the observations of SEM-EDS images, it is verified that spherical substances consist of a lot of carbon and a little bit of Sb (Fig. S2). Associated with a dosage of glucose, it is considerable that formations of spherical substances related to the over adding amount of glucose.

The TEM measurements were further used to confirm the structures of Sb@rGO@NSC-0.3 (Fig. 3h–k). Fig. 3j demonstrates the Sb particles in sizes around 20–30 nm are covered by the carbons thoroughly, suggesting that the Sb dispersed in carbon substrates very well. The Sb particles in nano sizes are beneficial to accelerate reaction kinetics for storing Li^+ [24]. Additionally, the HRTEM images are indicative of that lattice spacing (0.311 nm) corresponding to the (012) plane of Sb is suggestive of that the Sb exists in the Sb@rGO@NSC-0.3 as an efficacious evidence (Fig. 3k).

The general survey spectra of XPS are used to analyze the chemical states of Sb@rGO@NSC-X materials. As shown in Fig. S3, the peaks of C, N, O, S and Sb elements are observed at 285.6 eV, 399.6 eV, 530.6 eV, 228.6 eV (S 2 s), 164.6 eV (S 2p), 814.6 eV (Sb $3p_{1/2}$), 769.6 eV (Sb $3p_{3/2}$), 539.6 (Sb 3d) and 34.6 eV (Sb 4d) respectively. After carrying out the fitting of C1s, the peaks of 284.8 eV, 285.6 eV and 289.0 eV respectively corresponding to the C—C, C—N and C=O or C-S groups are observed distinctly (Fig. 4a) [29]. Fig. 4b describes the fitting peaks of N1s. It is obvious that the peaks of pyridinic N, pyrrolic N and quaternary N are 398.7 eV, 400.7 eV and 401.9 eV, respectively, and their ratios of peak areas are 38.6%, 34.8% and 26.6%, respectively, revealing that pyridinic N and pyrrolic N occupy a large proportion. This characteristic will induce numerous extrinsic defects and active sites for rapid ion diffusion and enhancing the electrochemical performance (Fig. 4b) [33]. In the S 2p fitting peaks, the peaks belonging to the S $2p_{1/2}$, S $2p_{3/2}$ and C-SO_x-C bonds are observed at 164.1 eV, 165.3 eV and 168.4 eV, respectively (Fig. 4c) [27]. The Sb $3d_{5/2}$ and Sb $3d_{3/2}$ are observed at 530.5 eV and 539.7 eV, respectively. An existence of O 1 s (531.9 eV) in the fitting peaks of Sb 3d indicates that the Sb oxides exist in the minority of the Sb@rGO@NSC-0.3 material (Fig. 4d) [24]. The XPS results suggest that the N,S-doping processes tremendously performed in carbonization processes.

BET methods described the porous structures of Sb@rGO@NSC-X materials in detail (Figs. 4e, f and S4). The N_2 adsorption-desorption isotherms of Sb@rGO@NSC-X materials can all be classified as type-IV isotherms with H3 hysteresis loops, indicating a lot of mesoporous exist in the Sb@rGO@NSC-X materials (Figs. 4e, f and S4) [34]. It is different from other materials, the micropores existing in the Sb@rGO@NSC-0.3 material causes that it possesses a bigger specific surface area (125.97 m^2/g) and pore volume than the others (Fig. 4f and Table S3). Therefore, the hierarchical porous structures lead Sb@rGO@NSC-0.3 to possess the tremendous electrochemical performance.

According to general electrochemical evaluations, the electrochemical performance of Sb, rGO/NSC, Sb@rGO@NSC-0.1, Sb@rGO@NSC-0.3 and Sb@rGO@NSC-0.5 were investigated

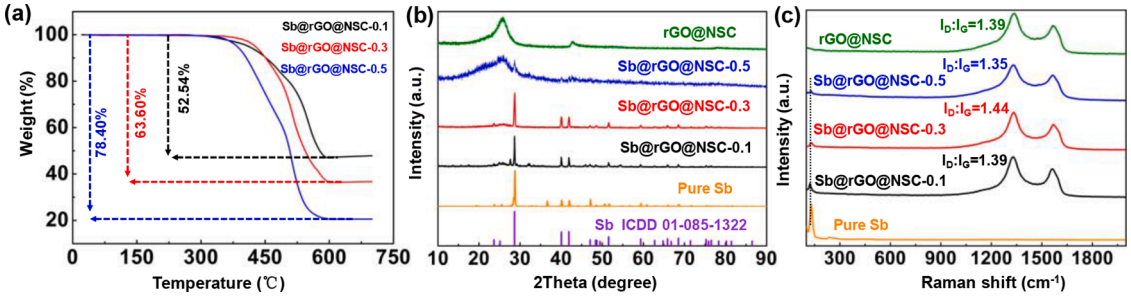

Fig. 2. TGA curves of Sb@rGO@NSC materials (a). XRD patterns of Sb, rGO/NSC and Sb@rGO@NSC materials (b). Raman results of Sb, rGO/NSC and Sb@rGO@NSC (c).

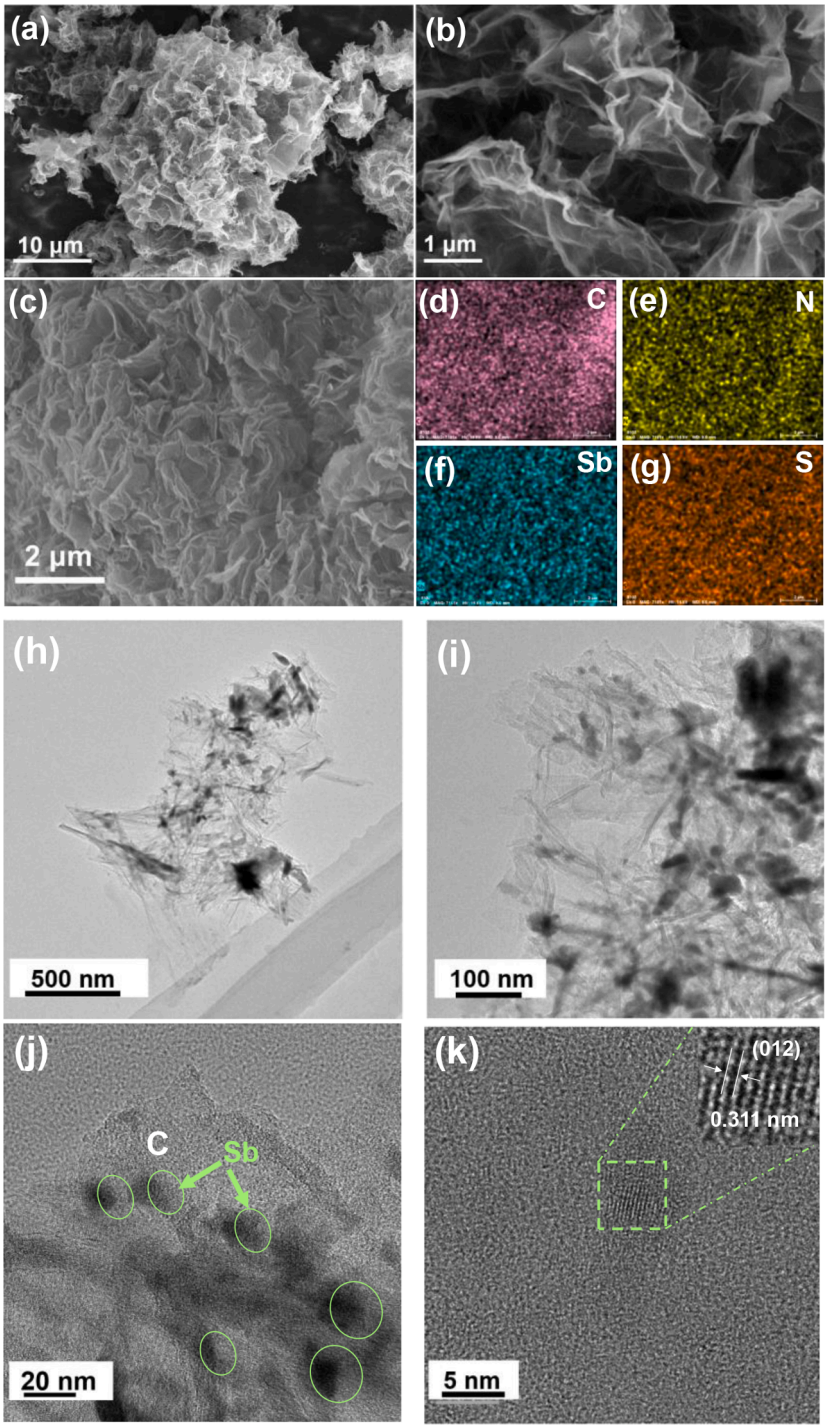

Fig. 3. SEM images of Sb@rGO@NSC-0.3 (a-c) and EDS images of Sb@rGO@NSC-0.3 (d-g). TEM images of (h, i) and HRTEM images of Sb@rGO@NSC-0.3 (j, k).

thoroughly. It is clear that the Sb, rGO/NSC, Sb@rGO@NSC-0.1, Sb@rGO@NSC-0.3 and Sb@GO@NSC-0.5, respectively exhibit the storage capacity (102.4 mAh g^{-1}, 429.7 mAh g^{-1}, 914.2 mAh g^{-1}, 1151.3 mAh g^{-1} and 756.6 mAh g^{-1}) at 0.1 A g^{-1} over 100 cycles, revealing that the Sb@rGO@NSC-0.3 possesses the much higher storage capacity than other materials (Fig. 5a). The storage tendency (first reduce and then increase) of Sb@rGO@NSC-0.3 is considered as follow. The formation of SEI can reduce the storage capacity firstly. Similar to report by Yhang et al., it is also considerable that structural conversions of Sb nano particles with the electrochemical activation may be a reason causing the increase tendency in the cycling performance (Fig. 5a) [35, 36].

Furthermore, the Sb@rGO@NSC-0.3 manifested extremely excellent storage capacity at big current densities. For instance, the storage capacity of Sb@rGO@NSC-0.3 has 1121.2 mAh g^{-1} at 0.5 A g^{-1}, after cycling 500 times (Fig. 5c). It is considerable that similar explanation of Fig. 5a is suitable to the Fig. 5c. Additionally, after cycling 1000 times, the storage performance of Sb@GO@NSC-0.3 were 721.1 mAh g^{-1} and 342.9 mAh g^{-1}, respectively corresponding to the current densities of 1 A g^{-1} and 5 A g^{-1} (Fig. 5d). The rate performance of materials were illustrated as show in Fig. 5b. It is clear to be aware of that Sb@rGO@NSC-0.3 possesses the more tremendous rate performance than other materials (Table S4). Based on a consideration of structure-activity relationship, the exceedingly excellent electrochemical

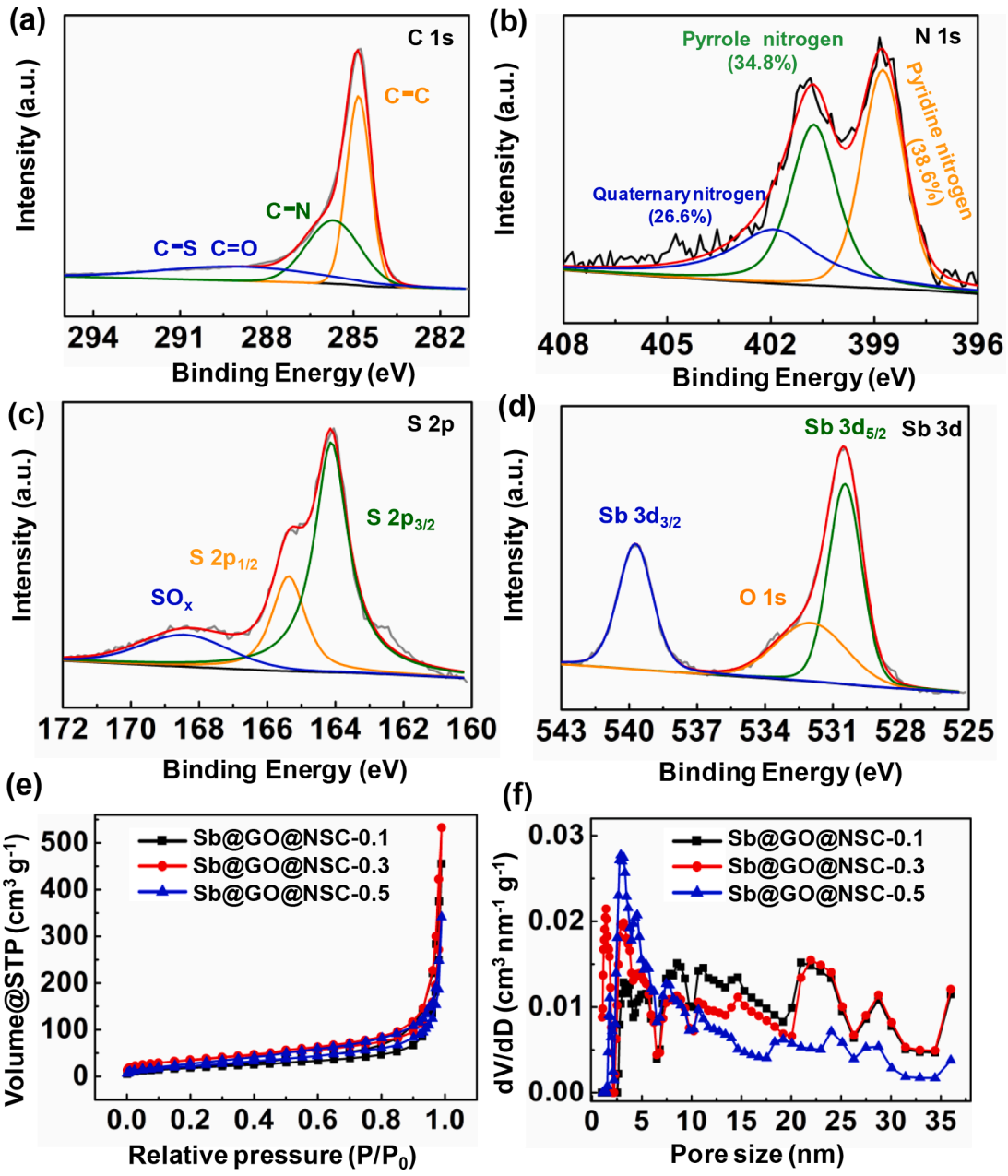

Fig. 4. Fitting results of C1s (a), N1s (b), S2p (c) and Sb3d (d) of the Sb@rGO@NSC-0.3 material. N_2 adsorption-desorption isotherms of Sb@rGO@NSC-X materials (e). Porous structures of Sb@rGO@NSC-X materials (f).

performance of Sb@rGO@NSC-0.3 are ascribed to its hierarchical pores structures (Fig. 5 and Table S3). In addition, the electrochemical performance of Sb@rGO@NSC-0.3 is better than any Sb anode electrodes reported so far, as shown in Table S5 [20,22,37,40–43].

The CV curves for the bare Sb and Sb@rGO@NSC-X materials are illustrated in Figs. 6a–d and S5 (a). As shown in Fig. 6a, a reductive peak of 0.6 V can be attributed to the formations of Li_3Sb and solid electrolyte interface (SEI) on the first cycle [24]. Likewise, this reductive peak was also observed in the first cycle of Sb@rGO@NSC-X materials (Fig. 6a–d). The oxidative peaks around 1.15 V of Sb and Sb@rGO@NSC-X materials are ascribed to the lithium deintercalation as a transformation from Li_3Sb to Sb [21,36]. In addition, with increasing the additional dosages of carbons, the oxidation-reduction peaks trend to be broad gradually (Figs. S5a and 6d). These CV results demonstrate the two contents of Sb and carbons in Sb@rGO@NSC-X materials participated in the electrochemical reactions completely (Figs. 6 a–d and S5a).

The charge-discharge results were depicted in Figs. 6 e–h and S5b. It can be seen that the initial coulombic efficiencies (ICE) of Sb, rGO/NSC, Sb@rGO@NSC-0.1, Sb@rGO@NSC-0.3 and Sb@rGO@NSC-0.5 are the 81.1%, 56.3%, 61.4%, 66.3% and 57.7%, respectively. The relatively low first coulombic efficiencies of Sb@rGO@NSC-X materials are generally attributed to the formations of (SEI) [20]. Besides, the Sb particles have a high ICE (81.1%) are probably attributed to their significantly small specific surface area (5.11 m^2/g) and pore volume (V_{toal}=0.007 $cm^3\ g^{-1}$) (Fig. S3 (c) and Table S3). In addition, as an alloy type of lithium storage, the reversible reaction on the first cycle proceeded completely, which is another possible reason causing a high ICE of Sb particles. Similar to Fig. 6e, the charge-discharge plateau is also observed in Fig. 6f–h, indicating that the Sb in Sb@rGO@NSC-X materials owns a contribution of storing Li^+. However, a similar plateau is not observed in Sb@rGO@NSC-0.5, which is ascribed to that the over existing of carbons causes the storage type being similar to carbon

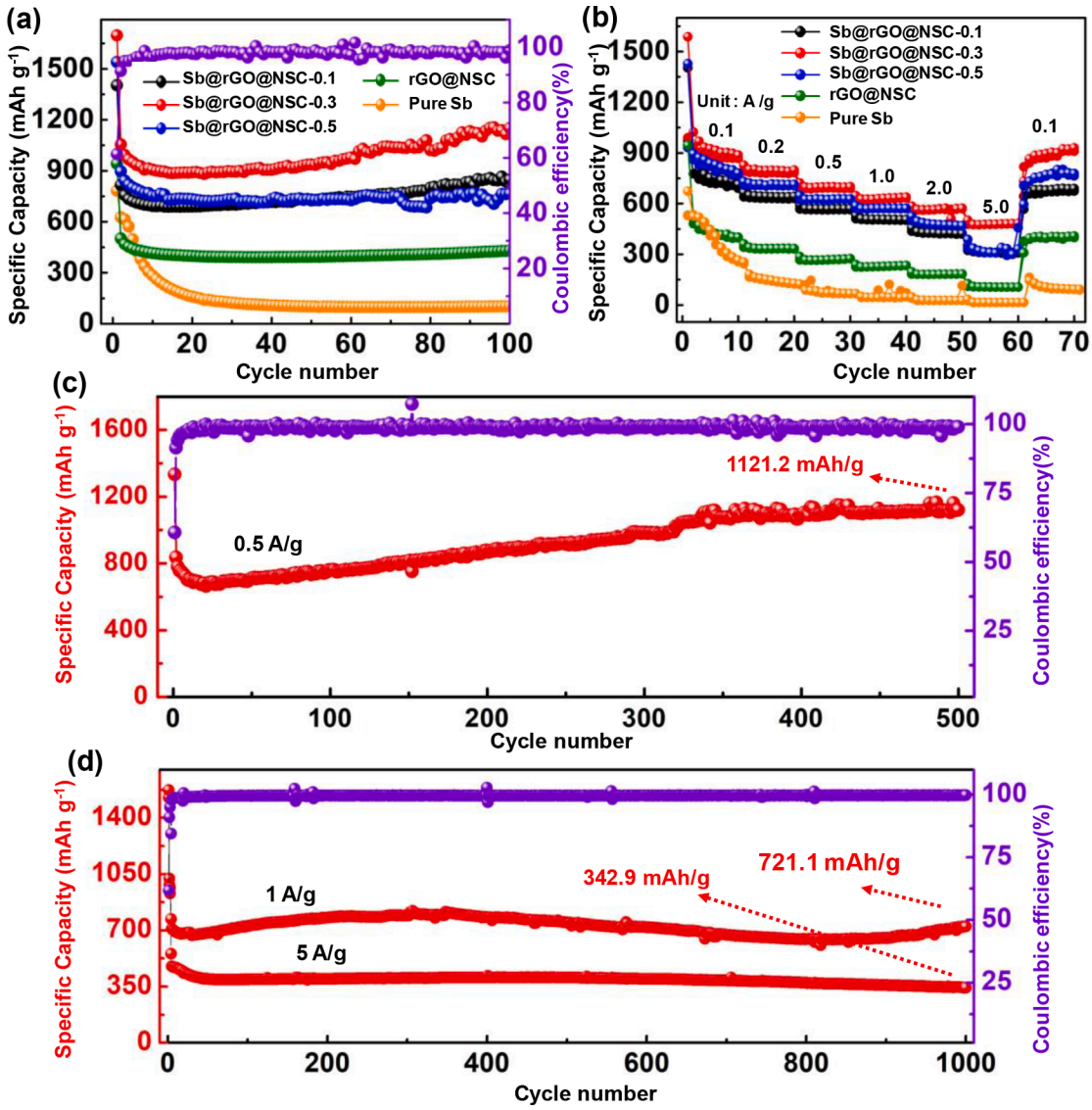

Fig. 5. Cycling performance of Sb, rGO/NSC and Sb@rGO@NSC-X materials (a). Rate performance of Sb, rGO/NSC and Sb@rGO@NSC-X materials (b). Long-term cycling stabilities of Sb@rGO@NSC-0.3 under high current densities (c, d).

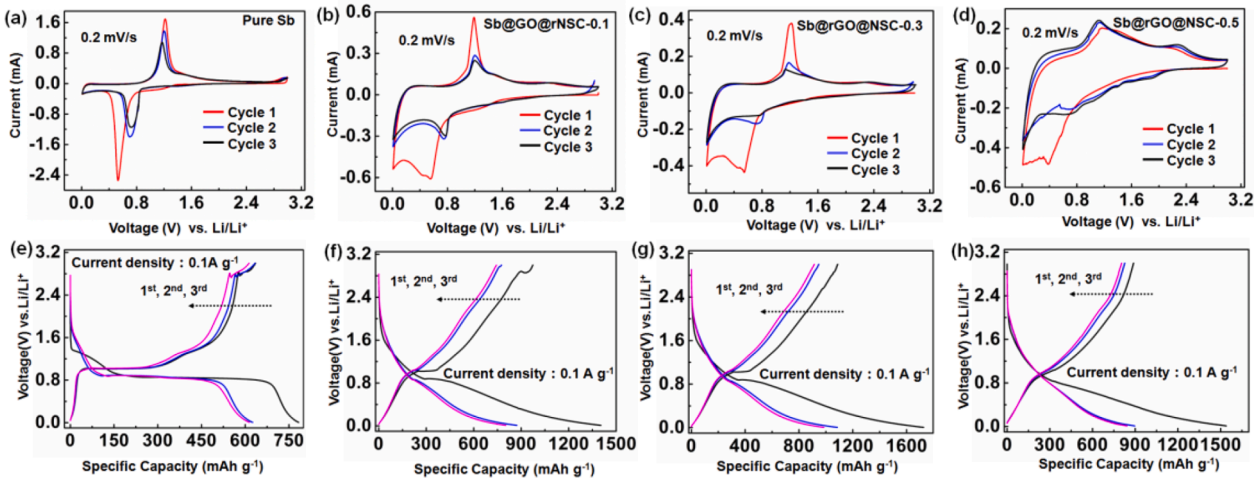

Fig. 6. CV curves of Sb (a) and Sb@rGO@NSC-X materials (b–d). Charge-discharge results of Sb (e), Sb@rGO@NSC-X materials (f–h).

materials (Fig. S5b). Similarly, the charge-discharge results can also reveal the participations of Sb and carbon materials in storing Li^+.

In order to explain the reason why the Sb@rGO@NSC-0.3 possesses more excellent electrochemical performance than other materials, the analyses of electrochemical impedance spectroscopy (EIS) were performed in detail. As shown in Fig. 7a, it is obvious that the Sb@GO@NSC-0.3 has smaller semicircle diameters than Sb, rGO/NSC, Sb@rGO@NSC-0.1 and Sb@rGO@NSC-0.5 materials, implying that Sb@rGO@NSC-0.3 possesses more excellent migration abilities than others [38,39]. On the basis of the equivalent circuit, the R_3 of Sb, rGO/NSC, Sb@rGO@NSC-0.1, Sb@rGO@NSC-0.3 and Sb@rGO@NSC-0.5 were calculated at 50.67 Ω, 160.8 Ω, 116.2 Ω, 48.7 Ω and 61.31 Ω, respectively (Fig. 7c).

Li^+ transformations were further evaluated by using the Warburg coefficient, as shown in Fig. 7b. The σ values can be calculated by Randles plots which are plotting of Z' with $\omega^{-1/2}$ ($\omega = 2\pi f$) in a low-frequency [29]. The larger σ values generally show the lower diffusion capacity. After calculations, the σ values of Sb, rGO/NSC, Sb@rGO@NSC-0.1, Sb@rGO@NSC-0.3, Sb@rGO@NSC-0.5 are 595.1 Ω $s^{1/2}$, 437.6 Ω $s^{1/2}$, 449.4 Ω $s^{1/2}$, 232.0 Ω $s^{1/2}$ and 363.7 Ω $s^{1/2}$, respectively, suggesting that Sb@rGO@NSC-0.3 owns more tremendous diffusion capacity than other materials [40,44]. Associating with the BET and SEM results, it is naturally considerable that the 3D hierarchical porous structures cause that the Sb@rGO@NSC-0.3 possesses the markedly impressive charge-transfer, leading it to have the high electrochemical performance [32].

As per Fig. 8, the storage mechanism of Sb@rGO@NSC-0.3 was eventually confirmed according to a method reported by Yang et al. [35]. After calculations, it is observed that the capacitive contributions occupy over 50%, even though the sweeping rates changed from 0.2 to 3 mV S^{-1} (Figs. 8b and S6). The increased capacitive effects can be ascribed to the contributions of two contents in Sb@rGO@NSC-0.3 completely, which is related to the formations of 3D hierarchical porous structures of Sb@rGO@NSC-0.3. In particular, the carbon contents play the role to restrict the volume expanding not only, but they can also provide the fast Li^+ migration channel, meanwhile, and attend to the Li^+ storing processes.

Finally, the ex-situ XPS measurements were carried out in detail, in order to investigate the conversions of chemical states of Sb@rGO@NSC-0.3 during the charge and discharge processes. Compared with the initial state, the new peak attributing to the Li_3Sb was observed at 528.4 eV, after discharged to 0.01 V (Fig. S7b) [45,46]. When charged to 3 V, the peak intensity of Li_3Sb decreased remarkably (Fig. S7c).

Meanwhile, the similar change was also observed in Li 1 s. After discharged to 0.01 V, the peak intensity of Li_3Sb (54.5 eV) became strong, and the same peak decreased remarkably, after charged to the 3 V [45]. On the basis of aforementioned analyses, the Li storage process can be inferred as $3Li^+ + 3e^- + Sb \leftrightharpoons Li_3Sb$ [47].

4. Conclusions

On the basis of double covering idea, the Sb@rGO@NSC having the high electrochemical performance is successfully prepared by using the $SbCl_3$, GO, glucose, ammonium citrate and sulfocarbamide. The tremendous dispersion of Sb particles in nano sizes and formations of 3D hierarchical porous structures of fabricated Sb@rGO@NSC-0.3 lead it to have excellent electrochemical performance. The storage capacity of Sb@rGO@NSC-0.3 is 1121.2 mAh g^{-1} at a current density of 0.5 A g^{-1} over cycling 500 times. Meanwhile, the Sb@GO@NSC-0.3 also exhibits the high storage capacity at high current densities. For instance, the Sb@rGO@NSC-0.3 composite delivers a remarkably reversible capacity of 721.1mAhg^{-1} with good cycling stability during 1000 cycles at 1 A g^{-1}. Even at 5 A g^{-1}, the capacity still reaches to 342.9mAh g^{-1}. In the storage mechanism, it is confirmed the fact that two contents in Sb@rGO@NSC-0.3 develop their storage abilities enough is a pivotal reason to make Sb@rGO@NSC-0.3 to have exceedingly fabulous electrochemical performance. Our studies can provide a referable case for the field fabricating materials with exceedingly high storage performance.

CRediT authorship contribution statement

Yuan Mu: Investigation, Data curation, Writing – original draft, Formal analysis, Methodology. **Dakui Zhang:** Investigation, Formal analysis, Methodology. **Jianke Li:** Investigation, Methodology. **Beibei Han:** Formal analysis. **Guiying Xu:** Data curation, Formal analysis, Methodology. **Kun Wang:** Data curation, Formal analysis, Conceptualization. **Baigang An:** Supervision. **Dongying Ju:** Supervision. **Lixiang Li:** Visualization. **Weimin Zhou:** Supervision, Conceptualization, Formal analysis, Writing – review & editing.

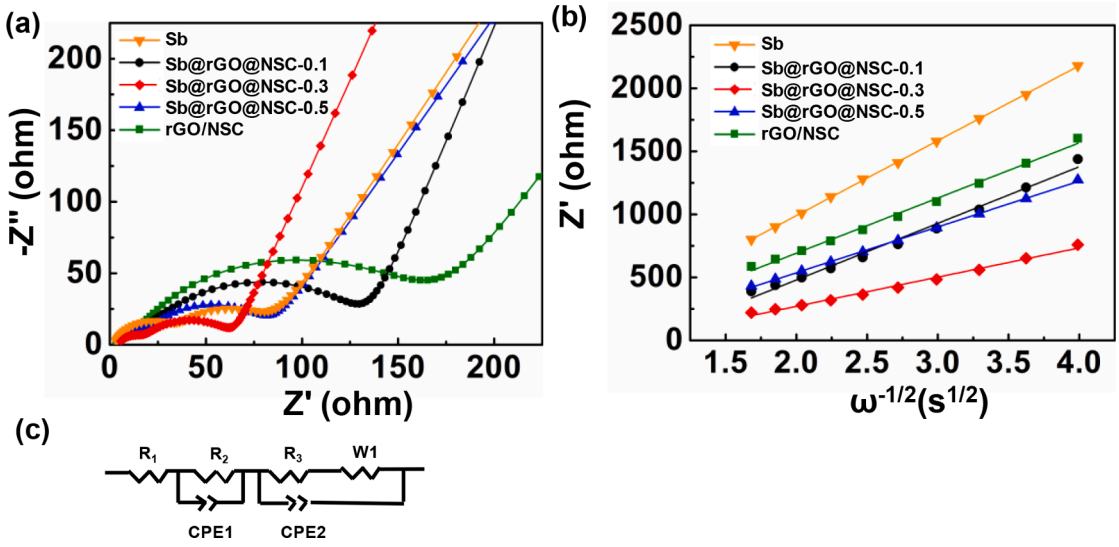

Fig. 7. Nyquist plot results (a), illustrations of relationships between Z′ and $\omega^{-1/2}$ in the low-frequency region (b) and the equivalent circuit model (c). Thereinto, R_1 is the total resistance of the electrolyte, separator, and electrical contacts; R_2 and R_3 are the Li^+ migration resistance through the SEI film and charge-transfer resistance, respectively; W1 is the Warburg impedance connected with the Li^+ diffusion process; CPE1and CPE2 represent the double layer resistance.

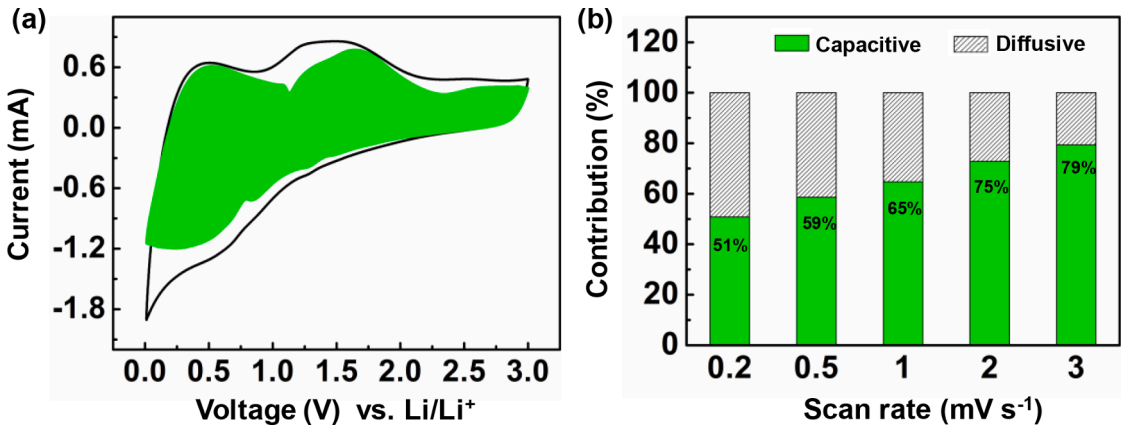

Fig. 8. The CV measurement result of Sb@rGO@NSC-0.3 at a scan rate of 3 mV s^{-1} (a). The bar charts showing the capacitive and diffusive contributions of Sb@rGO@NSC-0.3 at various scan rates (b).

Declaration of Competing Interest

The authors declare the following financial interests/personal relationships which may be considered as potential competing interests: Weimin Zhou reports was provided by University of Science and Technology Liaoning. Weimin Zhou reports a relationship with University of Science and Technology Liaoning that includes: employment. Weimin Zhou has patent No pending to No. No. The authors declare that they have no known competing financial interests or personal relationships that could have appeared to influence the work reported in this paper.

Data availability

No data was used for the research described in the article.

Acknowledgements

We are grateful to the support of University of Science and Technology Liaoning (601009816–39), LJKQZ2021126 and 2017RC03. This work obtains the support by the Liaoning Province Education Department of China (Grant No.601009887–16). This work is partly supported with the project supported by the National Natural Science Foundation of China (Grant No.51672117 and 51672118).

Supplementary materials

Supplementary material associated with this article can be found, in the online version, at doi:10.1016/j.electacta.2022.141532.

References

[1] V. Aravindan, Y. Lee, S. Madhavi, Research progress on negative electrodes for practical li-ion batteries: beyond carbonaceous anodes, Adv. Energy Mater. 5 (2015), 1402225.
[2] J. Hou, S. Qu, M. Yang, J. Zhang, Materials and electrode engineering of high capacity anodes in lithium ion batteries, J. Power Sources 450 (2020), 227697.
[3] Y. Cheng, Y. Sun, C. Chu, L. Chang, Z. Wang, D. Zhang, W. Liu, Z. Zhuang, L. Wang, Stabilizing effects of atomic Ti doping on high-voltage high-nickel layered oxide cathode for lithium-ion rechargeable batteries, Nano Res. 15 (2022) 4091–4099.
[4] K. Roy, A. Banerjee, S. Ogale, Search for new anode materials for high performance Li-Ion batteries, ACS Appl. Mater. Interfaces 14 (2022) 20326–20348.
[5] V. Etacheri, R. Marom, R. Elazari, D. Aurbach, Challenges in the development of advanced Li-ion batteries: a review, Energy Environ. Sci. 4 (2011) 3243–3262.
[6] J. Corsi, S. Welborn, E. Stach, E. Detsi, Insights into the degradation mechanism of nanoporous alloy-type Li-ion battery anodes, ACS Energy Lett. 6 (2021) 1749–1756.
[7] S. Yu, S. Lee, D. Lee, Y. Sung, T. Hyeon, Conversion reaction-based oxide nanomaterials for lithium ion battery anodes, Small 12 (2016) 2146–2172.
[8] F. Liu, Y. Liu, E. Wang, J. Ruan, S. Chen, Double-buffer silicon-carbon anode material by a dynamic self-assembly process for lithium-ion batteries, Electrochim. Acta 393 (2021), 139041.
[9] R. Zhu, Z. Wang, X. Hu, X. Liu, H. Wang, Silicon in hollow carbon nanospheres assembled microspheres cross-linked with n-doped carbon fibers toward a binder free, high performance, and flexible anode for lithium-ion batteries, Adv. Funct. Mater. 31 (2021), 2101487.
[10] S. Imtiaz, I. Amiinu, D. Storan, N. Kapuria, H. Geaney, T. Kennedy, K. Ryan, Dense silicon nanowire networks grown on a stainless-steel fiber cloth: a flexible and robust anode for lithium-ion batteries, Adv. Mater. 33 (2021), 2105917.
[11] L. Zhang, X. Liu, Q. Zhao, S. Dou, H. Liu, Y. Huang, X. Hu, Si-containing precursors for Si-based anode materials of Li-ion batteries: a review, Energy Storage Mater. 4 (2016) 92–102.
[12] Y. Lu, L. Yu, X. Lou, Nanostructured conversion-type anode materials for advanced lithium-ion batteries, Chem 4 (2018) 972–996.
[13] Y. Cheng, Q. Li, C. Wang, L. Sun, Z. Yi, L. Wang, Large-scale fabrication of core–shell structured C/SnO_2 hollow spheres as anode materials with improved lithium storage performance, Small 13 (2017), 1701993.
[14] D. Mhamane, V. Aravindan, D. Taneja, A. Suryawanshi, O. Game, M. Srinivasan, S. Ogale, Graphene based nanocomposites for alloy (SnO_2), and conversion (Fe_3O_4) type efficient anodes for Li-ion battery applications, Compos. Sci. Technol. 130 (2016) 88–95.
[15] S. Hwang, Q. Meng, P. Chen, K. Kisslinger, J. Cen, A. Orlov, Y. Zhu, E. Stach, Y. Chu, D. Su, Strain coupling of conversion-type Fe_3O_4 thin films for lithium ion batteries, Angew. Chem. Int. Ed. 56 (2017) 7813–7816.
[16] D. Jung, J. Jeong, S. Han, E. Oh, Electrochemical performance of potassium-doped wüstite nanoparticles supported on graphene as an anode material for lithium ion batteries, J. Power Sources 315 (2016) 16–22.
[17] Y. Cheng, S. Wang, L. Zhou, L. Chang, W. Liu, D. Yin, Z. Yi, L. Wang, SnO_2 quantum dots: rational design to achieve highly reversible conversion reaction and stable capacities for lithium and sodium storage, Small 16 (2020), 2000681.
[18] X. Ruan, Y. Yang, K. Pu, M. Gao, Y. Liu, H. Pan, Superior long-term cyclability of a nanocrystalline NiO anode enabled by a mechanochemical reaction-induced amorphous protective layer for Li-ion batteries, J. Power Sources 397 (2018) 134–142.
[19] H. Zhang, L. Wang, H. Li, X. He, Criterion for identifying anodes for practically accessible high-energy-density lithium-ion batteries, ACS Energy Lett. 6 (2021) 3719–3724.
[20] Z. Wang, J. Qu, S. Hao, Y. Zhang, F. Kong, D. Yang, Z. Yu, Sb nanoparticles embedded in a nitrogen-doped carbon matrix with tuned voids and interfacial bonds for high-rate lithium storage, ChemElectroChem 5 (2018) 2653–2659.
[21] Z. Wang, F. Zeng, D. Zhang, X. Wang, W. Yang, Y. Cheng, C. Li, L. Wang, Equably-dispersed Sb/Sb_2O_3 nanoparticles in ionic liquid-derived nitrogen-enriched carbon for highly reversible lithium/sodium storage, Electrochim. Acta 395 (2021), 139210.
[22] W. Luo, F. Li, J. Gaumet, P. Magri, S. Diliberto, L. Zhou, L. Mai, Bottom-up confined synthesis of nanorod-in-nanotube structured Sb@N-C for durable lithium and sodium storage, Adv. Energy Mater. 8 (2018), 1703237.
[23] J. He, Y. Wei, T. Zhai, H. Li, Antimony-based materials as promising anodes for rechargeable lithium-ion and sodium-ion batteries, Mater. Chem. Front. 2 (2018) 437–455.
[24] P. Feng, Z. Cui, S. He, Q. Liu, J. Zhu, C. Xu, R. Zou, J. Hu, Reversible formation of networked porous Sb nanoparticles during cycling: Sb nanoparticles encapsulated in a nitrogen-doped carbon matrix with nanorod structures for high-performance Li-ion batteries, J. Mater. Chem. A 7 (2019) 24292–24300.
[25] M. Schulze, R. Belson, L. Kraynak, A. Prieto, Electrodeposition of Sb/CNT composite films as anodes for Li-and Na-ion batteries, Energy Storage Mater. 25 (2020) 572–584.
[26] J. Zheng, Y. Wu, Y. Tong, Y. Sun, H. Li, Dual-carbon confinement strategy of antimony anode material enabling advanced potassium ion storage, J. Colloid Interface Sci. 622 (2022) 738–747.

[27] Z. Qiu, Y. Lin, H. Xin, P. Han, D. Li, B. Yang, P. Li, S. Ullah, H. Fan, C. Zhu, J. Xu, Ultrahigh level nitrogen/sulfur co-doped carbon as high performance anode materials for lithium-ion batteries, Carbon N. Y. 126 (2018) 85–92.
[28] L. Chen, X. He, H. Chen, S. Huang, M. Wei, N-Doped carbon encapsulating Bi nanoparticles derived from metal-organic frameworks for high-performance sodium-ion batteries, J. Mater. Chem. A 9 (2021) 22048–22055.
[29] M. Zheng, Y. Liu, Q. Ru, J. Zhang, Z. Pan, Y. Gao, F. Ling, L. Wei, Novel antimony phosphate loaded on grid-like N, S-doped carbon for facilitating sodium-ion storage, Chem. Eng. J. 415 (2021), 128942.
[30] J. Wang, J. Yang, W. Yin, S. Hirano, Carbon-coated graphene/antimony composite with a sandwich-like structure for enhanced sodium storage, J. Mater. Chem. A 5 (2017) 20623–20630.
[31] J. Qu, L. Yang, Z. Zhang, X. Xi, Honeysuckle-derived hierarchical porous nitrogen, sulfur, dual-doped carbon for ultra-high rate lithium ion battery anodes, J. Power Sources 333 (2016) 193–202.
[32] X. Zhu, J. Ye, Y. Lu, X. Jia, 3D graphene nanostructure composed of porous carbon sheets and interconnected nanocages for high-performance lithium-ion battery anodes and lithium–sulfur batteries, ACS Sustain. Chem. Eng. 7 (2019) 11241–11249.
[33] H. Wang, C. Yuan, R. Zhou, Q. Duan, Y. Li, Self-sacrifice template formation of nitrogen-doped porous carbon microtubes towards high performance anode materials in lithium ion batteries, Chem. Eng. J. 316 (2017) 1004–1010.
[34] J. Xu, Z. Liu, F. Zhang, J. Tao, L. Shen, X. Zhang, Bacterial cellulose-derived carbon nanofibers as both anode and cathode for hybrid sodium ion capacitor, RSC Adv. 10 (2020) 7780–7790.
[35] T. Yang, J. Zhong, J. Liu, Y. Yuan, D. Yang, Q. Mao, X. Li, Z. Guo, A general strategy for antimony-based alloy Nanocomposite embedded in Swiss-cheese-like nitrogen-doped porous carbon for energy storage, Adv. Funct. Mater. 31 (2021), 2009433.
[36] D. Zhang, J. Lu, C. Pei, S. Ni, Electrochemical activation, sintering, and reconstruction in energy-storage technologies: origin, development, and prospects, Adv. Energy Mater. 12 (2022), 2103689.
[37] J. Liu, L. Yu, C. Wu, Y. Wen, K. Yin, F. Chiang, R. Hu, J. Liu, L. Sun, L. Gu, J. Maier, Y. Yu, M. Zhu, New nanoconfined galvanic replacement synthesis of hollow Sb@C yolk-shell spheres constituting a stable anode for high-rate Li/Na-ion batteries, Nano Lett. 17 (2017) 2034–2042.
[38] K. Wang, D. Ju, G. Xu, Y. Wang, S. Chen, Zhang J, Y. Wu, W. Zhou, Study on electrochemical performances of composite carbon (FeO/C) materials fabricated by coal tar pitch and Fe_3O_4 particles, Int. J. Hydrog. Energy 44 (2019) 25199–25206.
[39] Y. Lee, K.Y. Lee, W. Choi, One-pot synthesis of antimony-embedded silicon oxycarbide materials for high-performance sodium-ion batteries, Adv. Fun. Mater. 27 (2017), 1702607.
[40] Y. Mao, R. Chen, H. You, Y. Liu, S. Luan, L. Hou, F. Gao, Advanced performance of S and N co-doped Sb@ CNFs with a 3D conductive network as superior lithium-ion battery anodes, J. Alloys Compd. 904 (2022), 164000.
[41] W. Yin, W. Chai, K. Wang, W. Ye, Y. Rui, B. Tang, Facile synthesis of Sb nanoparticles anchored on reduced graphene oxides as excellent anode materials for lithium-ion batteries, J. Alloys Compd. 797 (2019) 1249–1257.
[42] X. Yang, J. Ma, H. Wang, Y. Chai, R. Yuan, Partially reduced Sb/Sb_2O_3@ C spheres with enhanced electrochemical performance for lithium ion storage, Mater. Chem. Phys. 213 (2018) 208–212.
[43] Y. Wu, Q. Pan, F. Zheng, X. Ou, C. Yang, X. Xiong, M. Liu, D. Hu, C. Huang, Sb@ C/expanded graphite as high-performance anode material for lithium ion batteries, J. Alloys Compd. 744 (2018) 481–486.
[44] X. Li, J. Qu, H. Xie, Q. Song, G. Fu, H. Yin, An electro-deoxidation approach to co-converting antimony oxide/graphene oxide to antimony/graphene composite for sodium-ion battery anode, Electrochim. Acta 332 (2020), 135501.
[45] A. Hu, W. Chen, X. Du, Y. Hu, T. Lei, H. Wang, L. Xue, Y. Li, H. Sun, Y. Yan, J. Long, C. Shu, J. Zhu, B. Li, X. Wang, J. Xiong, An artificial hybrid interphase for an ultrahigh-rate and practical lithium metal anode, Energy Environ. Sci. 14 (2021) 4115–4124.
[46] A. Wang, J. Li, M. Yi, Y. Xie, S. Chang, H. Shi, L. Zhang, M. Bai, Y. Zhou, Y. Lai, Z. Zhang, Stable all-solid-state lithium metal batteries enabled by ultrathin LiF/Li_3Sb hybrid interface layer, Energy Storage Mater. 49 (2022) 246–254.
[47] L. Dashairya, D. Das, P. Saha, Binder-free electrophoretic deposition of Sb/rGO on Cu foil for superior electrochemical performance in Li-ion and Na-ion batteries, Electrochim. Acta 358 (2020), 136948.